

# Journal of Biomedical Optics

BiomedicalOptics.SPIEDigitalLibrary.org

## **Imaging depth and multiple scattering in laser speckle contrast imaging**

Mitchell A. Davis  
S. M. Shams Kazmi  
Andrew K. Dunn

# Imaging depth and multiple scattering in laser speckle contrast imaging

Mitchell A. Davis,<sup>a</sup> S. M. Shams Kazmi,<sup>b</sup> and Andrew K. Dunn<sup>b,\*</sup>

<sup>a</sup>The University of Texas at Austin, Department of Electrical and Computer Engineering, Austin, Texas 78712, United States

<sup>b</sup>The University of Texas at Austin, Department of Biomedical Engineering, Austin, Texas 78712, United States

**Abstract.** Laser speckle contrast imaging (LSCI) is a powerful and simple method for full field imaging of blood flow. However, the depth dependence and the degree of multiple scattering have not been thoroughly investigated. We employ three-dimensional Monte Carlo simulations of photon propagation combined with high resolution vascular anatomy to investigate these two issues. We found that 95% of the detected signal comes from the top 700  $\mu\text{m}$  of tissue. Additionally, we observed that single-intravascular scattering is an accurate description of photon sampling dynamics, but that regions of interest (ROIs) in areas free of obvious surface vessels had fewer intravascular scattering events than ROI over resolved surface vessels. Furthermore, we observed that the local vascular anatomy can strongly affect the depth dependence of LSCI. We performed simulations over a wide range of intravascular and extravascular scattering properties to confirm the applicability of these results to LSCI imaging over a wide range of visible and near-infrared wavelengths. © The Authors. Published by SPIE under a Creative Commons Attribution 3.0 Unported License. Distribution or reproduction of this work in whole or in part requires full attribution of the original publication, including its DOI. [DOI: [10.1117/1.JBO.19.8.086001](https://doi.org/10.1117/1.JBO.19.8.086001)]

Keywords: speckle; biomedical optics; simulations.

Paper 140102R received Feb. 20, 2014; revised manuscript received May 15, 2014; accepted for publication Jun. 23, 2014; published online Aug. 4, 2014.

## 1 Introduction

Recently, laser speckle contrast imaging (LSCI) has received increased attention as a method for full-field imaging of blood flow *in vivo* with high temporal resolution.<sup>1,2</sup> LSCI is performed through wide-field illumination of the tissue surface with a red or near-infrared (NIR) coherent light source and imaging of the resulting laser speckle pattern with a camera. Some of the photons scatter dynamically from moving particles, which causes a decorrelation, or blurring, of the laser speckle pattern. This decorrelation can be quantified by generating a contrast image by calculating the standard deviation divided by the mean over a small sliding window.<sup>3</sup> Although the technique of using LSCI to measure blood flow has been around for many years, it has been widely adopted over the past decade due to its simplicity, low instrumentation cost, and ability to produce images of relative blood flow changes with excellent spatial resolution.<sup>4,5</sup>

Despite the widespread use of the technique, the sampling depth and the degree of multiple scattering of LSCI are not well characterized. The unknown sampling depth has led to ambiguity regarding what vasculature is being sensed by the technique. The unknown degree of multiple scattering has led to several widely used models that relate the measured speckle contrast to speckle decorrelation times, and these models require assumptions about single or multiple dynamic scattering.<sup>6-9</sup>

LSCI is a wide-field imaging method, and therefore the measured contrast signal at any given region of interest (ROI) represents a volume of sampled tissue. The interpretation of the relative speckle contrast values in different areas of an image relies on understanding both the sampling volume as well as the number of dynamic scattering events. The purpose of this

work is to determine both the sampling volumes and the amount of intravascular (i.e., dynamic) scattering that occurs when using LSCI to measure flow in the cortex.

The challenge of characterizing these quantities stems from the fact that the contrast signal is generated from dynamic scattering. As these dynamic scattering events occur inside vessels, and vessels comprise only a small fraction of the total tissue volume, accurately modeling the dynamic scattering analytically is not possible. A numerical photon migration technique that can separate the intravascular scattering events from the extravascular scattering events is required. Furthermore, such a model must include a realistic description of the complex microvascular structure in the tissue.

Modeling photon migration numerically has recently become possible due to increased computational power and three-dimensional (3-D) Monte Carlo simulations using tissue-mimicking geometries.<sup>10-12</sup> In Monte Carlo simulations, the statistical pathways of photons can be simulated by the scattering coefficient, the absorption coefficient, the anisotropy, and the scattering phase function.<sup>13</sup> To model the LSCI imaging in the brain, 3-D voxelized geometries of brain microvasculature can be used in conjunction with the Monte Carlo technique to generate spatial probability distributions of photon travel inside vessels. The sampling depth and the degree of multiple scattering can then be derived from the probability distributions of photon travel in the intravascular space.

## 2 Three-Dimensional Monte Carlo Model

A 3-D Monte Carlo method was used to simulate photon propagation in an arbitrary geometry.<sup>14</sup> Geometries were specified by setting tissue optical properties in a 3-D voxelized grid. Due to the complexity of the geometry, many photons must be used to achieve statistical convergence of the photon path distributions. However, since each launched photon is statistically independent, many simulations can be simultaneously initialized as

\*Address all correspondence to: Andrew K. Dunn, E-mail: [adunn@utexas.edu](mailto:adunn@utexas.edu)

long as the random number generators produce statistically independent values. Parallelization of the code was performed using the message passing interface (MPI).<sup>15</sup> Using MPI, Monte Carlo simulations could be simultaneously initialized on an arbitrary number of processor cores. The scalable parallel pseudorandom number generator was used to ensure statistical independence among the parallel simulation instances.<sup>16</sup> This method allowed very large (10,000+ processor-hour) simulations to be performed quickly on the Texas Advanced Computing Center (TACC) supercomputers with only minor modifications to the unparallelized version of the software. This is in contrast to several recently reported graphics processing unit (GPU) adaptations of the Monte Carlo algorithm, which require much more extensive code modification to implement but in return allow a high amount of parallelization on a desktop computer.<sup>17,18</sup>

## 2.1 Geometry and Optical Properties

The model geometry was derived from *in vivo* images of mouse cortical vasculature. *In vivo* scanning two-photon fluorescence microscopy was used to generate depth-resolved stacks of microvasculature in a mouse (CD-1; male, 25 to 30 g). All experimental procedures were approved by the Institutional Animal Care and Use Committee at The University of Texas at Austin. The animals were anesthetized by inhalation of

2% to 3% isoflurane in oxygen through a nose cone. Body temperature was maintained at 37°C using a feedback-controlled heating plate (ATC100, World Precision Instruments, Sarasota, Florida) during the experiment. The animals were fixed in a stereotaxic frame (Kopf Instruments, Tujunga, California) and a 3 × 3 mm<sup>2</sup> portion of the skull was removed using a dental burr (Ideal™ Micro-Drill, Fine Science tools, Foster City, California). Figure 1(a) shows a speckle contrast image of flow in the mouse cortex. A 50-μL bolus of 5% weight/volume Texas Red (Invitrogen, Eugene, Oregon) was administered by retro-orbital injection to label the vasculature.

Four overlapping 600 × 600 μm<sup>2</sup> image stacks were taken in 2-μm axial steps down to 500 μm. The image stacks were stitched together using the method developed by Preibisch et al.<sup>19</sup> to create one large 1024 × 1024 × 500 μm<sup>3</sup> image stack. The stack was then extended down to 900 μm in depth by matching vascular volume fractions to 3% to 6% as reported in McCaslin et al.<sup>20</sup> by replicating the capillary bed layers already present between 250 and 450 μm in the image stack. The geometry extension was done because the tissue absorption coefficients in the LSCI wavelength range are low, so more room was needed to allow the photons to scatter down into the geometry and then return to the surface. The geometry for the Monte Carlo model was then created by filtering the images to smooth out imaging artifacts in the

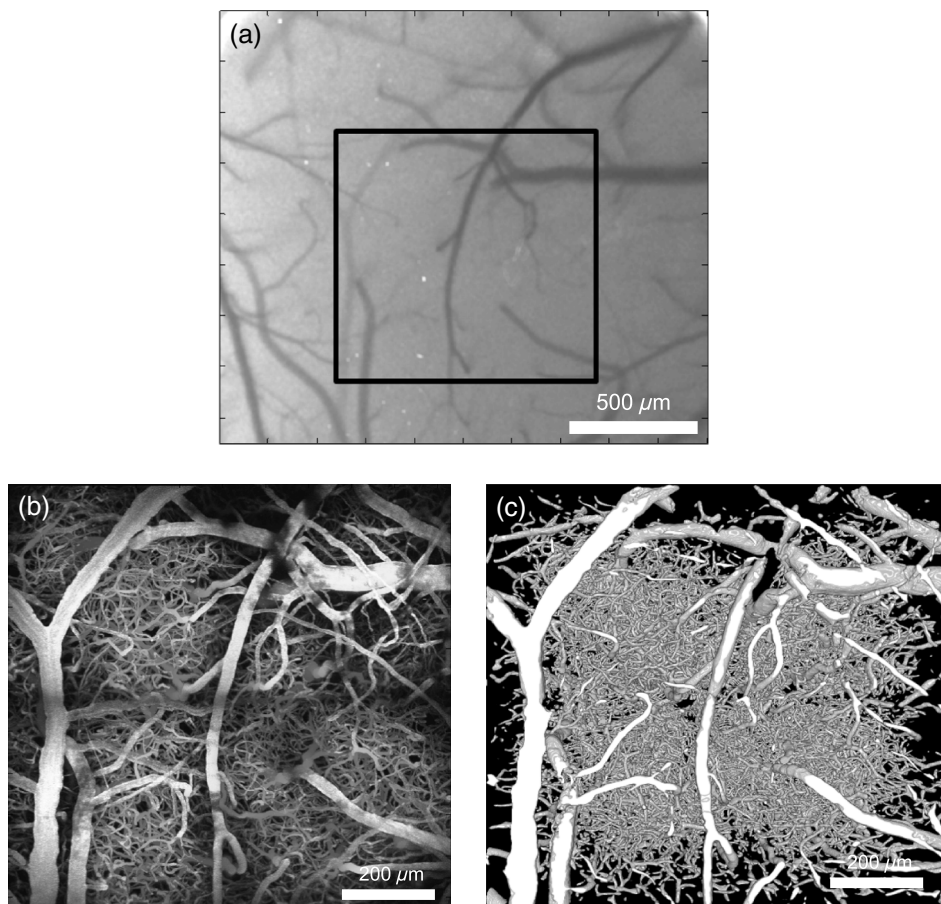


**Fig. 1** (a) Laser speckle contrast imaging (LSCI) image of mouse cortex. Region of interest (ROI) indicates location of two photon imaging for vascular geometry. (b) 1024 μm by 1024 μm wide by 500 μm deep microvasculature image stack acquired by two-photon scanning microscopy from the area shown in the LSCI image. (c) Three-dimensional rendering of segmented geometry used for Monte Carlo simulations.

vasculature, interpolating to attain images at every  $1 \mu\text{m}$  and thresholding the images to generate a  $1024 \times 1024 \times 900$  voxel binary geometry. Figure 1(b) shows a maximum intensity image of the combined two-photon stacks, whereas Fig. 1(c) shows a 3-D rendering of the segmented geometry used in the Monte Carlo simulations. Each voxel was assigned optical properties based on whether it represented extravascular or intravascular space.

The intravascular absorption coefficients were generated based on the extinction coefficients of hemoglobin. The concentration of hemoglobin in the vasculature was assumed to be 2.3 mM.<sup>21</sup> The range of intravascular scattering coefficients was interpolated from measurements done by Bevilacqua et al.,<sup>22</sup> Friebel et al.,<sup>23</sup> and Meinke et al.<sup>24</sup> Extravascular absorption and scattering coefficients were based on the *in vitro* measurements by Yaroslavsky et al.<sup>25</sup> It was necessary to use *in vitro* measurements of the extravascular tissue because blood was assumed to only be present in the intravascular space. The *in vitro* measurements were taken in the absence of blood. Table 1 lists the optical properties used in these simulations. Upper and lower ranges on the intra- and extravascular scattering coefficients correspond to the maximum and minimum scatterings seen in the visible and NIR range of 600 to 850 nm at normal hematocrit levels ( $\sim 15\%$  to  $45\%$ ), which is the typical range of wavelengths used for the LSCI imaging.

## 2.2 Photon Simulation

Photons entered the geometry at a slightly diverging angle ( $\text{NA} = 0.01$ ) in a  $900\text{-}\mu\text{m}$ -diameter circle centered in the middle-top of the geometry. The photon scattering angle was determined using the Henyey–Greenstein phase function. The photon weight was calculated using Beer’s law in conjunction with the cumulative photon travel distance and the absorption coefficient in each tissue type. In our simulations, every photon scattering event was recorded for photons exiting the top of the sample (i.e., reflected photons) for use in postprocessing. This was done in order to record the spatial distribution of intravascular scattering events. An ROI was selected on the surface to determine the depth-dependent intravascular scattering distribution, as well as the number of times the photon scattered inside vessels corresponding to a given detector size and location. As previously mentioned, the LSCI signal is determined by the dynamic interaction between the photons and the moving erythrocyte scatterers. As such, the depth dependence considers only the scattering events that occur inside vessels.

## 2.3 Depth-Dependent Intravascular Scattering

The depth-dependent signal distribution,  $f(z)$ , which is the probability of an intravascular scattering events occurring at depth  $z$  in the geometry, was calculated by integrating the absorption-weighted scattering events in  $x$  and  $y$ , and then normalizing

$$f(z) = \frac{\iint \sum_i w_i N_i(x, y, z) dx dy}{\iiint \sum_i w_i N_i(x, y, z) dx dy dz}, \quad (1)$$

where  $w_i$  is the absorption-weighted value of photon  $i$ , and  $N_i(x, y, z)$  is the number of times photon  $i$  has scattered in vessels through the voxel corresponding to  $x, y, z$ . The photon weight  $w_i$  was calculated using the following relation:

$$w_i = \prod_j \exp(-\mu_a^j l_{ij}), \quad (2)$$

where  $\mu_a^j$  is the absorption coefficient of tissue-type  $j$ , and  $l_{ij}$  is the path length of photon  $i$  through tissue-type  $j$ . In our simulation, the tissue type,  $j$ , was either blood vessel or extravascular tissue (Table 1).

The depth-integrated signal distribution,  $F(z)$ , can then be calculated by integrating  $f(z)$  from 0 to  $z$  and represents the amount of intravascular scattering which occurs in the top  $z \mu\text{m}$  in the geometry. The expression for  $F(z)$  is as follows:

$$F(z) = \int_0^z f(z) dz. \quad (3)$$

## 2.4 Multiple Scattering

The number of intravascular scattering events was determined by counting the number of times each photon scattered inside vessels during the Monte Carlo simulation. A histogram was created, and the absorption weighted value of each detected photon was added to the bin corresponding to the number of times that photon had scattered in vessels. The histogram was then normalized to produce a probability distribution of the amount of intravascular scattering.

## 2.5 Simulations

### 2.5.1 Effect of region of interest selection on scattering distributions

Our first consideration was to determine whether different regions of a speckle contrast image exhibit difference depth dependence and multiple scattering characteristics in a typical LSCI imaging setup. A  $900\text{-}\mu\text{m}$ -diameter, slightly diverging ( $\text{NA} = 0.01$ ) cone of light on the surface of the tissue geometry was used as the illumination. The intravascular optical properties were  $\mu_a = 0.2 \text{ mm}^{-1}$ ,  $\mu_s = 120 \text{ mm}^{-1}$ , and  $g = 0.98$ . Extravascular optical properties were  $\mu_a = 0.02 \text{ mm}^{-1}$ ,  $\mu_s = 10 \text{ mm}^{-1}$ , and  $g = 0.90$ . The ROIs were  $15 \times 15 \mu\text{m}^2$  squares representing single pixels in the LSCI image and were placed at several locations at the surface of the geometry, which represent both vasculature and parenchyma in the LSCI image shown in Fig. 1(a). In this context, parenchyma is defined as high-contrast regions of the LSCI image that do not appear to be vessels.

### 2.5.2 Effect of optical properties on scattering distributions

Two ROIs were chosen to examine the effects of optical properties on photon sampling. To determine the effect of the intravascular scattering coefficient, the extravascular  $\mu_s$  was held constant at  $10 \text{ mm}^{-1}$ , whereas the intravascular scattering coefficient was varied between 60, 80, 100, and  $120 \text{ mm}^{-1}$ . The

**Table 1** Optical properties for microvasculature geometry.

	$\mu_a$ ( $\text{mm}^{-1}$ )	$\mu_s$ ( $\text{mm}^{-1}$ )	$g$
Intravascular	0.20	60 to 120	0.98
Extravascular	0.02	5 to 15	0.90

depth-integrated scattering distribution and the distribution of dynamic scattering events were calculated for comparison.

The effect of the extravascular scattering coefficient was examined by holding the intravascular scattering coefficient constant at  $120 \text{ mm}^{-1}$  and varying the extravascular coefficient between 5, 10, and  $15 \text{ mm}^{-1}$ .

### 3 Results

#### 3.1 Dependence of Intravascular Scattering on Microvascular Geometry

Figure 2 shows the effect of ROI selection on the depth-integrated and depth-dependent vascular scattering. The  $15 \mu\text{m}$  colored boxes overlaid onto the maximum intensity projection in Fig. 2(a) correspond to the matching color plot lines in Figs. 2(c) and 2(d). In Fig. 2(d), each curve represents the probability that a photon from a particular ROI will scatter inside a blood vessel at a given depth. The probability values in Figs. 2(c) and 2(d) correspond to a  $\Delta z$  of  $1 \mu\text{m}$ . Intravascular optical properties were  $\mu_a = 0.20 \text{ mm}^{-1}$ ,  $\mu_s = 120 \text{ mm}^{-1}$ , and  $g = 0.98$ . Extravascular optical properties were  $\mu_a = 0.02 \text{ mm}^{-1}$ ,  $\mu_s = 10 \text{ mm}^{-1}$ , and  $g = 0.90$ .

Figure 2(c) demonstrates that the distribution of intravascular scattering near the surface is strongly dependent on the distribution of surface vasculature near the ROI. For example, the light blue ROI overlying a surface vessel in the bottom right of the geometry has over 50% of the intravascular scattering events occurring in the top  $30 \mu\text{m}$  of the geometry. The dark blue ROI over the microvascular cluster in the top left of the

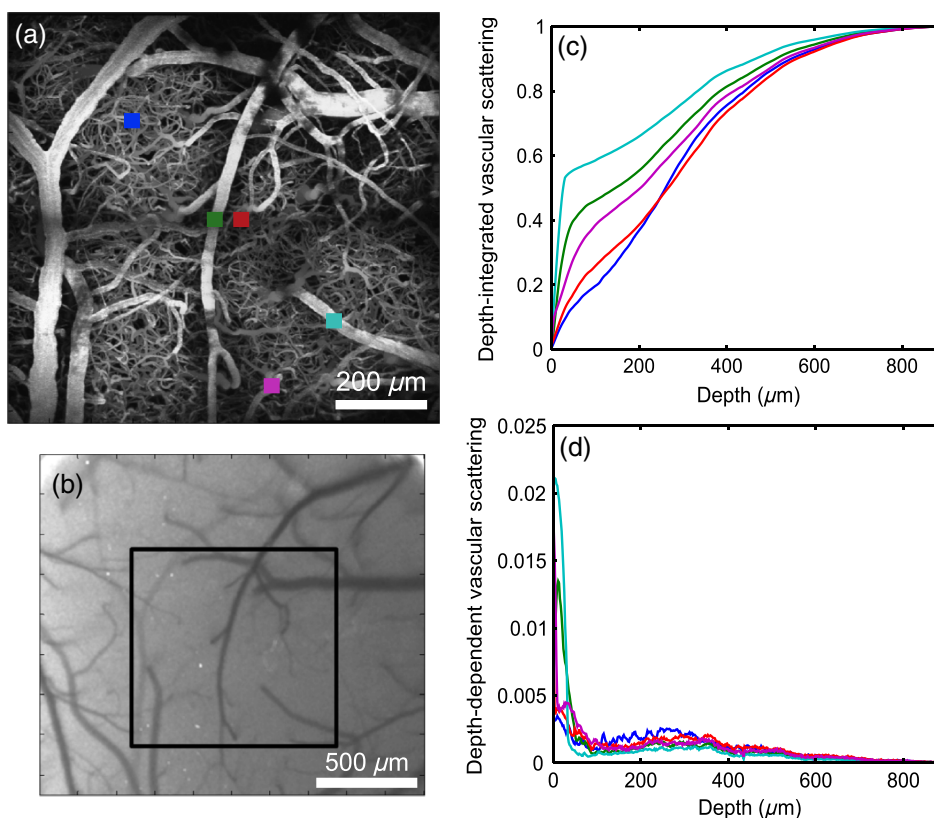
geometry has less than 10% of the total intravascular scattering events occurring in the top  $30 \mu\text{m}$  of the geometry. The green ROI is positioned over a vessel that is  $\sim 10 \mu\text{m}$  into the tissue, which explains the rise in the depth-dependent scattering at that level. The depth dependent scattering from the purple ROI shows a rapid drop in the first  $10 \mu\text{m}$  because of the small vessel size. However, there is more scattering in the 20- to  $60\text{-}\mu\text{m}$  range than the blue or red ROI because of the descending branch of the vessel.

Below the first  $300 \mu\text{m}$ , the pattern of intravascular scattering in Figs. 2(c) and 2(d) is similar for all ROI. This suggests that the depth dependence of intravascular scattering beyond  $300 \mu\text{m}$  is not dependent on the vascular anatomy beneath the ROI, but rather on the depth into the tissue and the volume fraction of vasculature in the tissue at that depth.

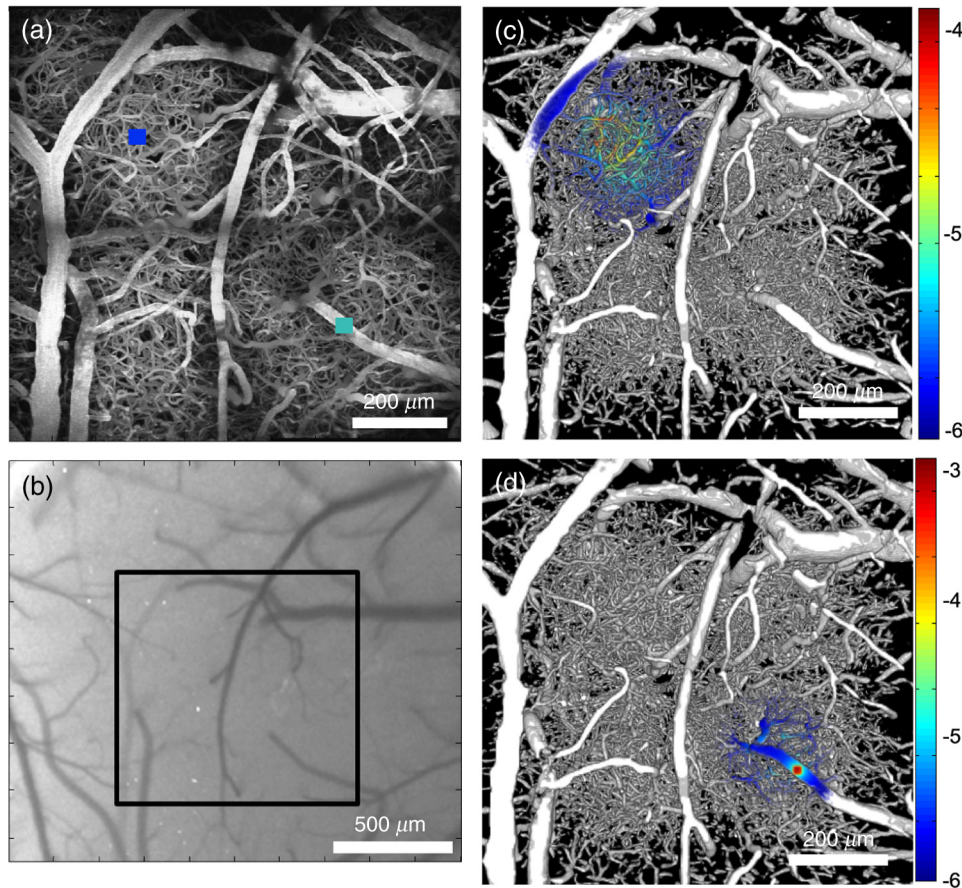
#### 3.2 Scattering Characteristics of Surface Vasculature and Parenchyma

Figure 3 shows the characteristics of vascular scattering for two of the ROI shown in Fig. 2. Figures 3(a) and 3(b) show the maximum intensity projection of the tissue vasculature with the ROI marked by square  $15\text{-}\mu\text{m}$  boxes, as well as the corresponding LSCI. The ROI in the top left corresponds to parenchyma in the speckle contrast image from Fig. 1, whereas the bottom right ROI corresponds to a resolved surface vessel.

Figures 3(c) and 3(d) show a 3-D rendering of the intravascular scattering events in each  $2 \times 2 \times 2 \mu\text{m}^3$  region of the geometry. Though photons scattered and changed directions



**Fig. 2** Comparison of depth-dependent and depth-integrated scattering characteristics at different ROIs. (a) Maximum intensity projection of two-photon stack with color overlays corresponding to  $15 \mu\text{m} \times 15 \mu\text{m}$  ROI; (b) the depth-dependent scattering distributions corresponding to detector positions marked in (a); (c) depth-integrated scattering distributions corresponding to ROI marked in (a).



**Fig. 3** (a) Maximum intensity projection of two-photon stack with  $15\ \mu\text{m} \times 15\ \mu\text{m}$  ROIs corresponding to the parenchyma (a) and surface vessel (d); (b) is the LSCI image with an ROI corresponding to the location of the two-photon image stack; (c and d) a log-scale color overlay of dynamic scattering in the geometry in the parenchyma (c) and the surface vessel (d) ROI using intravascular  $\mu_s = 120\ \text{mm}^{-1}$ .

outside of vessels, only the intravascular events are relevant to LSCI imaging, and therefore the extravascular events are not displayed. Photon scattering detected at the parenchyma ROI are evenly spread over a larger area of tissue, and a larger number of vessels, than the photon scattering detected at the surface arteriole. The scattering in the surface vessel ROI in Fig. 3(d) is primarily inside the vessel directly under the detected area, though the scattering volume also includes the some of the descending part of the arteriole. Once the arteriole branches into capillaries, the scattering distribution begins to spread out into the nearby vessels.

To provide an idea of the degree of spatial localization of the vascular scattering, the area surrounding the ROI corresponding to 50% of the collected signal was calculated. In the surface vessel ROI, a  $40 \times 40 \times 40\text{-}\mu\text{m}^3$  cube with the top-center of the cube centered in the middle of the ROI contained  $\sim 50\%$  of the total intravascular scattering events. In the parenchyma ROI, however, the size of the cube had to be expanded to  $400 \times 400 \times 400\ \mu\text{m}^3$  to contain 50% of the total intravascular scattering events.

This simple comparison demonstrates the vast difference in spatial sampling that is achieved when considering different regions of the image. This is not primarily due to reduced scattering outside of the ROI in the case of the vessel ROI, but instead is due to increased scattering events occurring near the ROI region. In fact, the photons reaching the surface vessel

ROI experienced  $\sim 65\%$  more intravascular scattering events on average than photons reaching the parenchyma ROI. Additionally, the fraction of the total scattering attributed to intravascular scattering was different in the parenchyma (27%) and surface vessel (40%) ROIs.

### 3.3 Effect of Optical Scattering Properties on Depth Dependence and Multiple Scattering

Figures 4(a) and 4(b) show the LSCI image and maximum intensity projection with parenchyma and surface vessel ROI. The effect of changing the intravascular scattering coefficient on the number of dynamic scattering events and depth-dependent intravascular scattering distributions can be seen in Figs. 4(c)–4(e) for the parenchyma ROI and Figs. 4(f)–4(h) for the surface vessel ROI.

Figures 4(c) and 4(d), 4(f) and 4(g) show histograms of the number of intravascular scattering events that the photons arriving at each ROI undergo while scattering through the geometry. The parenchyma ROI in Figs. 4(c) and 4(d) is more strongly weighted toward single scattering, while the surface vessel ROI in Figs. 4(f) and 4(g) is more strongly weighted toward multiple scattering. As expected, the number of dynamic scattering events show an approximately linear dependence on the intravascular scattering coefficient due to the high intravascular anisotropy.

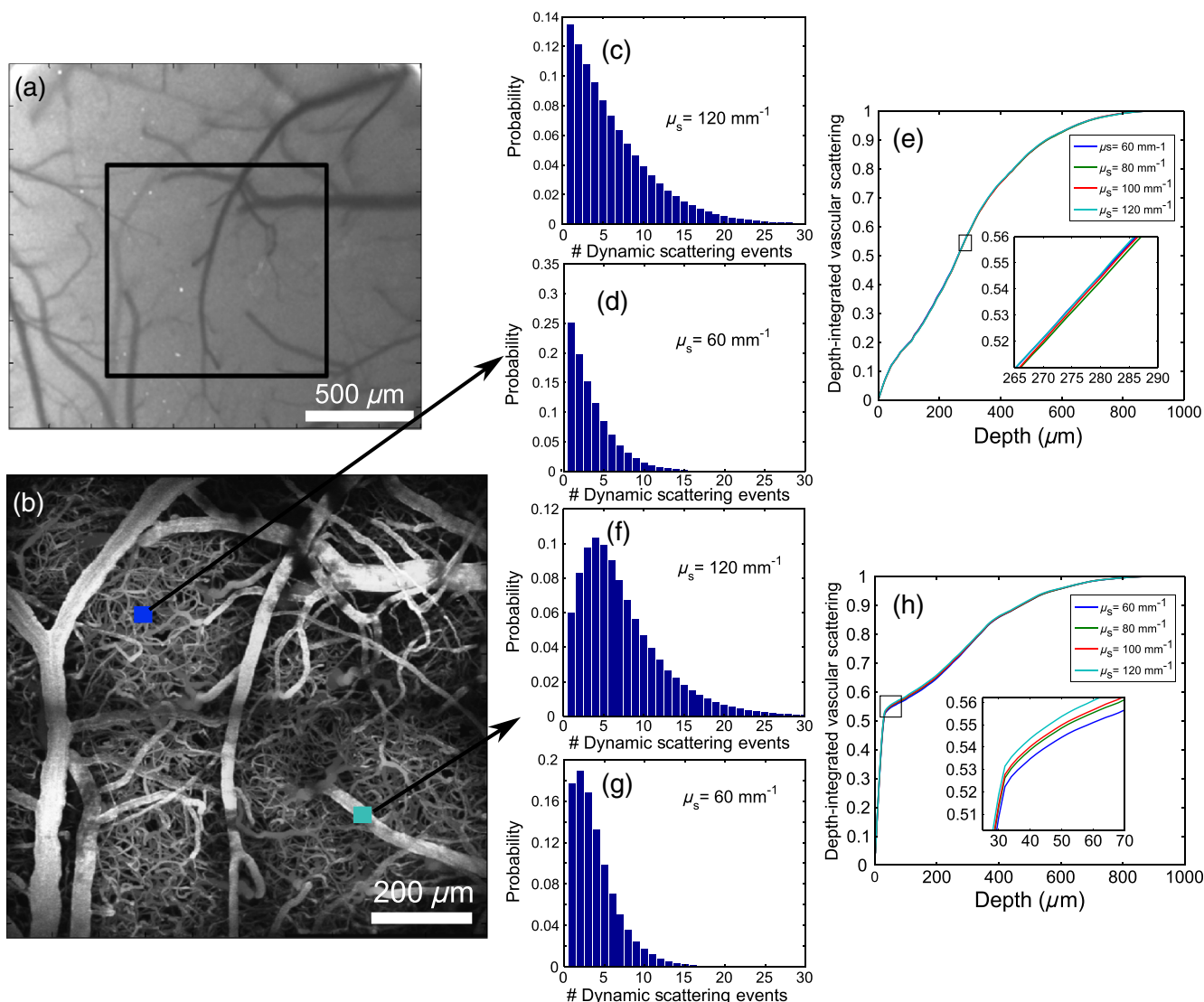


**Fig. 4** In-depth examination of surface vessel ROI and parenchyma ROI location, showing the effect of changing intravascular scattering coefficient. (a) LSCI image with an ROI corresponding to the location of the two-photon image stack. (b) Maximum intensity projection of two-photon stack with  $15 \times 15 \mu\text{m}^2$  ROIs corresponding to the parenchyma (a) and surface vessel (b); (c–e) the effect of changing the intravascular scattering coefficient on the distribution of dynamic scattering events (c and d) and the depth-integrated scattering distribution (e); (f–h) the effect of changing intravascular scattering coefficient for a surface vessel ROI.

Figures 4(e) and 4(h) show the effect of changing the intravascular scattering coefficient on the depth-integrated scattering. The results show that changing intravascular scattering coefficient causes a negligible change in the relative depth-dependent scattering distributions in both the parenchyma and the surface vessels. This suggests that our results should hold over a wide range of wavelengths, blood oxygenation fractions, and hematocrit (Hct) values.

The effect of extravascular scattering coefficient can be seen in Fig. 5. The intravascular scattering coefficient is  $120 \text{ mm}^{-1}$ . Figures 5(b) and 5(c) show the depth-integrated scattering distribution in the parenchyma and the surface vessel ROI when the extravascular  $\mu_s = 5 \text{ mm}^{-1}$ ,  $10 \text{ mm}^{-1}$ , and  $15 \text{ mm}^{-1}$ . The results show that changing the scattering coefficient from  $5 \text{ mm}^{-1}$  to  $15 \text{ mm}^{-1}$  causes a slight reduction in the sampling depth. In the surface vessel ROI in Fig. 5(b), the scattering attributed to the surface vessel increases by 2% over the

range of extravascular scattering coefficients. The parenchyma ROI in Fig. 5(b) shows an increase in depth-integrated vascular scattering of over 5% at depths of 100 to 600  $\mu\text{m}$ .

Figures 5(d) and 5(e) show the difference in the distribution of intravascular scattering events in the parenchyma ROI. The results demonstrate that increasing the extravascular scattering coefficient causes a negligible increase in single scattering. Figures 5(f) and 5(g) show the distribution of dynamic scattering events when the ROI is positioned over the surface vessel. In this case, the amount of single scattering decreases slightly as the extravascular scattering coefficient is increased. The probability of scattering 4 to 8 times, however, appears to increase slightly as the extravascular scattering coefficient is increased. Although slight changes in scattering were observed, overall the results suggest that changing the extravascular scattering coefficient has little effect on the number of dynamic scattering events.

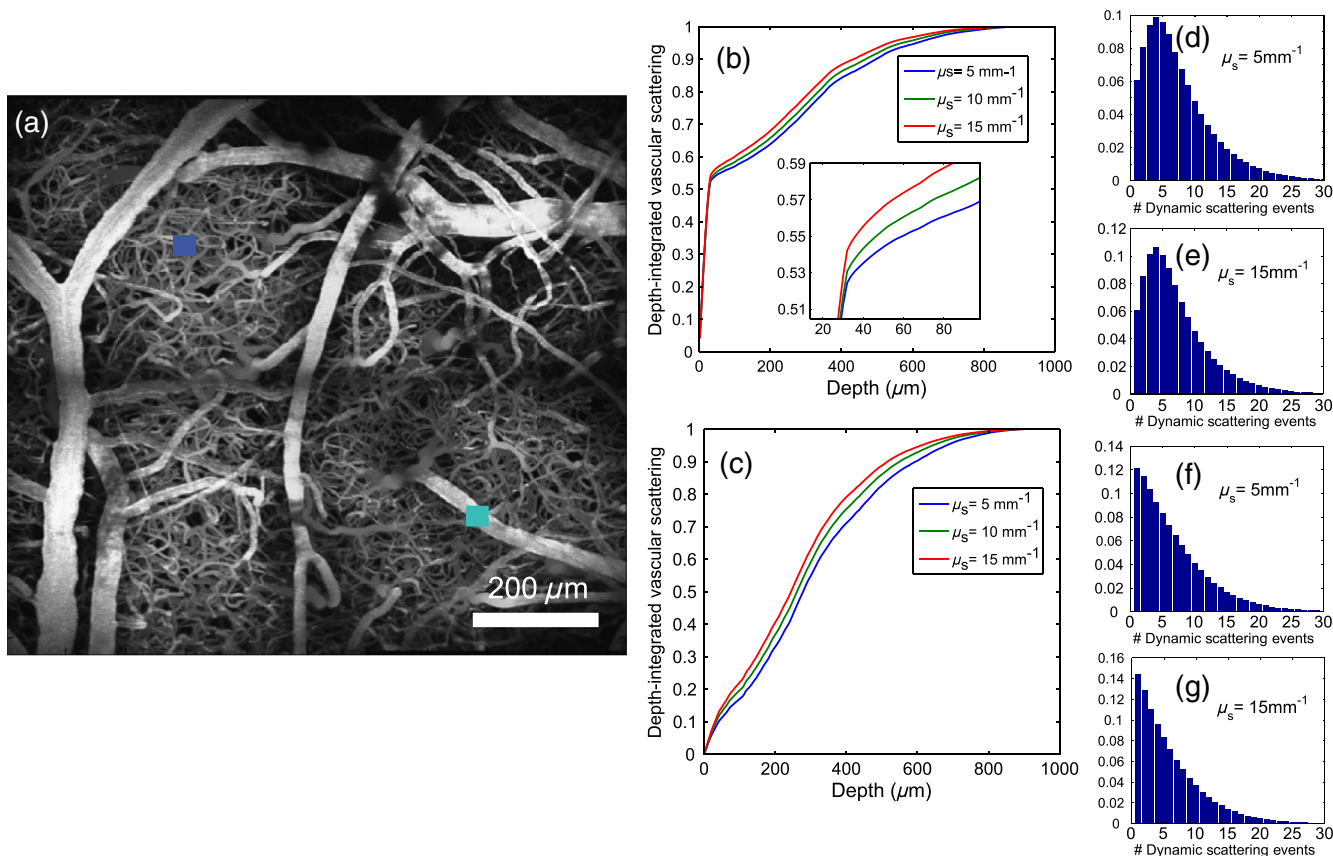


**Fig. 5** The effect of changing the extravascular scattering coefficient. (a) Maximum intensity projection of two-photon stack with  $15 \times 15 \mu\text{m}^2$  ROIs corresponding to the parenchyma (top left) and surface vessel (top right) locations; (b and c) are the depth-integrated scattering distribution in the surface vessel (b) and parenchyma (c); (d and e) are the number of dynamic scattering events in the parenchyma when the extravascular  $\mu_s$  is  $5 \text{ mm}^{-1}$  (d) and  $15 \text{ mm}^{-1}$  (e); (f and g) are the same as (d and e), but correspond to the surface vessel ROI.

## 4 Discussion

### 4.1 Computational Considerations

We performed several convergence tests to determine the validity of the presented scattering distributions. Convergence was determined by comparison to a  $3 \times 10^{11}$  photon simulation. The number of photons simulated was reduced until the average mean-squared error of the depth-dependence calculation exceeded  $1 \times 10^{-8}$ . To demonstrate convergence of the depth-dependent and depth-integrated scattering distributions,  $6 \times 10^9$  photons were required. These simulations were run on the TACC Lonestar machine and required approximately 550 CPU hours to complete. Because of the code parallelization, the simulations required slightly over 2 h of wall clock time to run on 240 cores.

For the visualization of the 3-D scattering distributions in Figs. 3(c) and 3(d), a larger number of simulated photons were required to produce a smoothly rendered 3-D image. For these simulations,  $3 \times 10^{11}$  photons were simulated. These simulations were run on 2400 cores for  $\sim 17$  h, for a total of 40,000 processor hours, or about 4.5 processor years. The capability to run these simulations was the result of MPI parallelization of the Monte Carlo code. This was a simple affair, as there is no need for between-thread communication due to the independence of stochastic photon simulations. At the end of

each run, the results from each thread were combined to attain the statistical power required for convergence of the scattering distributions.

### 4.2 Depth Dependence of Detected Photons

As only a single vascular anatomy was used to generate the results shown, it is difficult to claim that any given imaging scenario will result in a specific imaging depth for a given ROI. However, the results do show trends in the spatial distribution of intravascular scattering that seem to be invariant of the ROI. Figure 2 demonstrates that regardless of ROI position, there is a significant amount of vascular scattering below the surface vasculature in the cortex. Across all ROI, we found that the top 700 μm of tissue accounts for over 95% of the detected signal. Previous modeling studies of two-dimensional reflectance imaging in the brain have reported that 97% of the signal originates from the top 500 μm of the cortex when tissue is assumed to be homogeneous.<sup>26</sup> The slight difference between these results highlights the effect of considering only dynamic, intravascular scattering events as “signal.”

Not only does the detected signal represent vascular scattering far beneath the surface, it also represents scattering laterally in space. The depth-dependence plot shown in Fig. 2(d) shows that the parenchyma ROI has some scattering in the top 30 μm of the tissue. However, there are no surface vessels in that region

below the ROI, so all dynamic scattering at those depths occurred spatially offset from the selected ROI. This can be seen in the rendered representation of that ROI in Fig. 3(c). This has little effect on the overall signal when considering a surface vessel, as the amount of scattering inside the vessel strongly outweighs any contribution from lateral regions. In the parenchyma region, however, lateral surface scattering accounted for almost 15% of the total dynamic scattering events. A change in speckle contrast value in the parenchyma will therefore represent a large integrated volume both in depth and laterally on the surface.

### 4.3 ROI Position Dependence Reduced Below 300 $\mu\text{m}$

The results in Fig. 2 suggest that the location of the ROI has a strong impact on the first 300  $\mu\text{m}$  of the depth-dependent and depth-integrated distribution. When the ROI is over a surface vessel, as much as 50% to 60% of the collected signal corresponded to scattering in the top 50  $\mu\text{m}$  of the geometry. However, when placed over unresolved vasculature (parenchyma), as little as 10% of the signal originated in the top 50  $\mu\text{m}$ . This has a couple of implications for speckle contrast imaging in the cortex. First, it means that the contrast values corresponding to resolved vessels do not solely represent the resolved vessel in the image. Other vessels in the first 300  $\mu\text{m}$  below the resolved vessel also contribute to the signal.

In addition, the depth-dependent scattering distribution beyond 300  $\mu\text{m}$  is nearly the same regardless of ROI location. At these depths, the volume fraction of vasculature determines the amount of scattering. This is because the intravascular scattering distribution spreads out spatially as with increasing depth into the tissue.

The vascular anatomy also plays a significant role in the distribution of scattering events. For example, in Fig. 3(d), the scattering events appear to track or follow the descending arteriole. This is because there are very few other vessels in the vicinity of those descending arterioles until about 200  $\mu\text{m}$  into the tissue. As a result, nearly all of the vascular scattering from the first 200  $\mu\text{m}$  can be attributed to the resolved arteriole. Combining this observation with the possibility of increased surface vessel sensitivity would allow for a signal that is strongly weighted toward the intravascular scattering events occurring in the single-surface arteriole.

### 4.4 Multiple Scattering

The primary conclusion from the intravascular scattering distributions shown in Figs. 4(c), 4(d), 4(f), 4(g) and 5(d)–5(g) is that the majority of collected photons experience multiple intravascular scattering events. This contradicts the assumptions made in models where the assumption of single scattering is made on the basis of highly diffuse vascularization.<sup>6</sup> Even when imaging in the parenchyma and taking the lowest scattering coefficient, as in Fig. 4(d), single-scattered photons accounted for less than 25% of the detected signal. The results here support the concerns brought up in a recent paper by Briers et al.,<sup>27</sup> which claimed on a theoretical basis that the single-scattering assumption is likely incorrect.

Additionally, the distribution of dynamic scattering events is also dependent on the ROI position. The ROI over parenchyma demonstrates an exponential distribution of dynamic scattering events. However, from Fig. 4(f), the surface vessel ROI

distribution is significantly different from the parenchyma ROI in the first eight dynamic scattering events, which corresponds to up to 60  $\mu\text{m}$  of intravascular travel. After the first eight events, the difference between the two distributions is much smaller. This makes some intuitive sense, as the maximum photon path length through the 30  $\mu\text{m}$  surface vessel would be around 60  $\mu\text{m}$ , so the difference between the two distributions should primarily be in the scattering events corresponding to 60  $\mu\text{m}$  or lower intravascular path lengths. This observation is important, as the speckle visibility models which do consider multiple scattering treat the scattering events as uncorrelated.<sup>7</sup> Although this assumption may hold when imaging in the parenchyma, it fails when considering imaging over surface vessels because the multiple sequential scattering events that occur in the surface vessel are highly correlated.<sup>28</sup>

It is worth noting that the scattering coefficient in capillaries is often reported to be lower than in larger vessels due to the reduced hematocrit. This may suggest that the scattering in the parenchyma resembles the lower scattering coefficient in Fig. 4(d), while when looking at surface vessels the distribution is closer to Fig. 4(f). This trend was confirmed by performing a simulation where the capillaries and noncapillaries were given Hct-adjusted scattering coefficients. The trends in multiple scattering held and suggest that the results in Figs. 4(c), 4(d), 4(f), and 4(g) provide approximate upper and lower bounds on multiple scattering in the cortex during LSCI.

### 4.5 Practical Implications for LSCI Imaging

The results shown here offer some insights that are useful for the interpretation of LSCI results. Figures 4 and 5 show that the choice of wavelength does not significantly affect the depth dependence or volumetric integration of the LSCI signal. Additionally, there is substantial evidence to suggest that processing should be different for parenchymal and surface vessel regions. Both the multiple scattering properties and the spatial extent of scattering are significantly different.

Although the speckle contrast signal is said to be proportional to the average velocity or flow sampled by the photons in the tissue, this approximation breaks down in the presence of multiple sequential scattering in a large vessel.<sup>2</sup> When multiple scattering is present, the contribution to the dynamic signal is proportional to the velocity difference between subsequent scattering events.<sup>29</sup> Therefore, when a photon scatters multiple times in a single vessel, the contribution of each scattering event to the dynamics is proportional to the change in blood velocity between subsequent scattering events (i.e., the velocity profile inside the vessel). The speckle contrast over surface vessels may then be a better representation of the relative motion in the surface vessel, rather than the mean velocity. In the parenchyma, on the other hand, most photons sample capillary vessels only once. The contribution to the dynamic signal is therefore proportional to the absolute velocity of blood flow in those vessels.

Furthermore, it has been suggested that with higher degrees of multiple scattering not only is estimation of a fluctuation as a fraction of the coherence factor  $\beta$  unreliable but the actual value of  $\beta$  may be reduced.<sup>30</sup> In this case, the lower contrast observed over surface vessels may not be only caused by increased motion sampling, but also by a reduction in  $\beta$ . This observation reinforces the need for separation of processing over surface vessels and parenchyma, or at least for processing schemes

where the value of  $\beta$  does not affect the estimated flow measurement.<sup>7,8</sup>

#### 4.6 Limitations

The primary limitation of this method is that it does not allow for the calculation of the effect of the dynamic scattering event on the LSCI signal. The dynamic signal generated at each scattering event is dependent on the scattering particle motion and the photon scattering angle. Previous methods of calculating the autocorrelation function have required the assumption of particle independence, which is valid either in the case of scattering particle diffusion or in the highly multiple scattering regime (i.e., diffusing wave spectroscopy/diffuse correlation spectroscopy).<sup>31</sup> As LSCI operates in the intermediate scattering regime, information about the direction and speed of flow inside the vasculature would be required to calculate the autocorrelation function.

Future work which includes the vector direction of particle movement in each vessel could be used to calculate the autocorrelation function and therefore measure the sensitivity of the LSCI signal to variations in flow throughout the vasculature. Such work would allow the determination of the effect of blood volume changes on the LSCI signal, as well as optimal exposure times and the effect of the multiple scattering on the interpretation of speckle contrast changes. The results of this work suggest a need for this future analysis, as the degree of scattering seen here falls into the intermediate range which is not well described by speckle contrast analysis methods which assume either single or diffuse scattering.<sup>32</sup>

#### 5 Conclusion

We found that the top 700  $\mu\text{m}$  of tissue accounts for over 95% of the intravascular scattering events. We found that the differences in depth dependence between detectors are mostly dependent on vascular anatomy in the top 300  $\mu\text{m}$  of tissue, while below 300  $\mu\text{m}$  it is dependent on the overall volume fraction of vessels. When considering the number of dynamic scattering events, we found that single scattering is an accurate representation of photon–vessel interactions. However, when considering large vessels, there is a significant amount of scattering that corresponds to photons scattering through the diameter of the vessel up to two times.

Future work which incorporates the dynamic interactions needs to be done to understand the sensitivity of LSCI to flow changes as a function of depth and distance from the image pixel. Additionally, including the dynamic changes will allow further examination of the impact of large surface vessels on the imaging of capillary/nutritive flow, as well as to access the accuracy of currently used models of speckle imaging.

#### Acknowledgments

We gratefully acknowledge support from the Consortium Research Fellows Program, NIH (EB-011556, NS-078791, NS-082518), NSF (CBET-0644638), American Heart Association (14EIA18970041), and the Coulter Foundation. The authors also acknowledge the Texas Advanced Computing Center (TACC) at the University of Texas at Austin for providing HPC resources that have contributed to the research results reported within this paper. URL: <http://www.tacc.utexas.edu>.

#### References

1. A. K. Dunn et al., "Dynamic imaging of cerebral blood flow using laser speckle," *J. Cereb. blood flow Metab.* **21**(3), 195–201 (2001).
2. D. A. Boas and A. K. Dunn, "Laser speckle contrast imaging in biomedical optics," *J. Biomed. Opt.* **15**(1), 011109 (2010).
3. J. D. Briers, G. Richards, and X. W. He, "Capillary blood flow monitoring using laser speckle contrast analysis," *J. Biomed. Opt.* **4**(1), 164–175 (1999).
4. A. Fercher and J. Briers, "Flow visualization by means of single-exposure speckle photography," *Opt. Commun.* **37**(5), 326–330 (1981).
5. J. Briers and S. Webster, "Laser speckle contrast analysis (LASCA): a non-scanning, full-field technique for monitoring capillary blood flow," *J. Biomed. Opt.* **1**(2), 174–179 (1996).
6. R. Bonner and R. Nossal, "Model of laser Doppler measurements of blood flow in tissue," *Appl. Opt.* **20**(12), 2097–2107 (1981).
7. R. Bandyopadhyay and A. Gittings, "Speckle-visibility spectroscopy: a tool to study time-varying dynamics," *Rev. Sci. Instrum.* **76**(9), 093110 (2005).
8. A. B. Parthasarathy et al., "Robust flow measurement with multi-exposure speckle imaging," *Opt. Express* **16**(3), 1975–1989 (2008).
9. S. M. S. Kazmi et al., "Chronic imaging of cortical blood flow using multi-exposure speckle imaging," *J. Cereb. Blood Flow Metab.* **6**(3), 798–808 (2013).
10. D. A. Boas et al., "Three dimensional Monte Carlo code for photon migration through complex heterogeneous media including the adult human head," *Opt. Express* **10**(3), 159–170 (2002).
11. M. A. Davis et al., "Depth dependence of vascular fluorescence imaging," *Biomed. Opt. Express* **2**(12), 3349–3362 (2011).
12. J. Barton et al., "Optical Monte Carlo modeling of a true portwine stain anatomy," *Opt. Express* **2**(9), 391–396 (1998).
13. S. Prahl et al., "A Monte Carlo model of light propagation in tissue," in *SPIE Proc. Dosim. Laser Radiat. Med. Biol.*, Vol. 1, pp. 102–111 (1989).
14. C. K. Hayakawa et al., "Perturbation Monte Carlo methods to solve inverse photon migration problems in heterogeneous tissues," *Opt. Lett.* **26**(17), 1335–1337 (2001).
15. W. Groop, E. L. Lusk, and A. Skjellum, *Portable Parallel Programming with the Message Passing Interface*, MIT Press, Cambridge (1999).
16. M. Mascagni and A. Srinivasan, "Algorithm 806: SPRNG: a scalable library for pseudorandom number generation," *ACM Trans. Math. Softw.* **26**(3), 436–461 (2000).
17. E. Alerstam, T. Svensson, and S. Andersson-Engels, "Parallel computing with graphics processing units for high-speed Monte Carlo simulation of photon migration," *J. Biomed. Opt.* **13**(6), 060504 (2008).
18. Q. Fang and D. Boas, "Monte Carlo simulation of photon migration in 3D turbid media accelerated by graphics processing units," *Opt. Express* **17**(22), 20178–20190 (2009).
19. S. Preibisch, S. Saalfeld, and P. Tomancak, "Globally optimal stitching of tiled 3D microscopic image acquisitions," *Bioinformatics* **25**(1), 1463–1465 (2009).
20. A. F. H. McCaslin et al., "In vivo 3D morphology of astrocyte-vasculature interactions in the somatosensory cortex: implications for neurovascular coupling," *J. Cereb. blood flow Metab.* **31**(3), 795–806 (2011).
21. F. E. Robles, S. Chowdhury, and A. Wax, "Assessing hemoglobin concentration using spectroscopic optical coherence tomography for feasibility of tissue diagnostics," *Biomed. Opt. Express* **1**(1), 310–317 (2010).
22. F. Bevilacqua et al., "In vivo local determination of tissue optical properties: applications to human brain," *Appl. Opt.* **38**(22), 4939–4950 (1999).
23. M. Friebe et al., "Optical properties of circulating human blood in the wavelength range 400–2500 nm," *J. Biomed. Opt.* **4**(1), 36–46 (1999).
24. M. Meinke et al., "Empirical model functions to calculate hematocrit-dependent optical properties of human blood," *Appl. Opt.* **46**(10), 1742–53 (2007).
25. A. N. Yaroslavsky et al., "Optical properties of selected native and coagulated human brain tissues in vitro in the visible and near infrared spectral range," *Phys. Med. Biol.* **47**(12), 2059–2073 (2002).
26. P. Tian et al., "Monte Carlo simulation of the spatial resolution and depth sensitivity of two-dimensional optical imaging of the brain," *J. Biomed. Opt.* **16**(1), 016006 (2011).

27. D. Briers et al., "Laser speckle contrast imaging: theoretical and practical limitations," *J. Biomed. Opt.* **18**(6), 066018 (2013).
28. S. A. Carp et al., "Due to intravascular multiple sequential scattering, diffuse correlation spectroscopy of tissue primarily measures relative red blood cell motion within vessels," *Biomed. Opt. Express* **2**(7), 2047–2054 (2011).
29. D. Bicoût, E. Akkermans, and R. Maynard, "Dynamical correlations for multiple light scattering in laminar flow," *J. Phys.* **1**(4), 471–491 (1991).
30. J. W. Goodman, "Statistical properties of laser speckle patterns," *Laser Speckle Relat. Phenom.*, Vol. 9, pp. 9–75 (1975).
31. D. Boas and A. Yodh, "Spatially varying dynamical properties of turbid media probed with diffusing temporal light correlation," *JOSA A* **14**(1), 192–215 (1997).
32. P. Zakharov and F. Scheffold, "Advances in dynamic light scattering techniques," *Light Scatt. Rev.*, pp. 433–467 (2009).

**Mitchell A. Davis** is a graduate student at the University of Texas at Austin. He received his BS and MS degrees in biomedical engineering and electrical engineering from the University of Texas at Austin in

2009 and 2011, respectively. His current research interests include laser-tissue interactions and dynamic light scattering.

**S. M. Shams Kazmi** is a postdoctoral fellow at the University of Texas at Austin, where he received his PhD in 2014 in the field of biomedical optics for monitoring vascular function, disease, and therapy. He received his BSE degree from Duke University in 2008 in biomedical and electrical engineering with an emphasis on medical devices and imaging. He is a member of SPIE.

**Andrew K. Dunn** is an associate professor of biomedical engineering and a fellow of the Herring professorship at the University of Texas at Austin. His research is in the field of optical microscopy for investigation of brain function, particularly in stroke and neurovascular disorders.